# Investigation of sessile droplet evaporation using a transient two-step moving mesh model

Xue Li, Brandon Murray, Shankar Narayan\*
Department of Mechanical, Aerospace, and Nuclear Engineering,
Rensselaer Polytechnic Institute, 110 8th Street, Troy, NY 12180
\*Corresponding author. E-mail address: narays5@rpi.edu. Telephone: 1-518-276-6988

#### **Abstract**

The evaporation of droplets on surfaces is a ubiquitous phenomenon essential in nature and industrial applications ranging from thermal management of electronics to self-assembly-based fabrication. In this study, water droplet evaporation on a thin quartz substrate is analyzed using an unsteady two-step arbitrary Lagrangian-Eulerian (ALE) moving mesh model, wherein the evaporation process is simulated during the constant contact radius (CCR) and contact angle (CCA) modes. The numerical model considers mass transfer in the gas domain, flow in the liquid and gas domains, and heat transfer in the solid, liquid, and gas domains. Besides, the model also accounts for interfacial force balance, including thermocapillary stresses, to obtain the instantaneous droplet shape. Experiments involving droplet evaporation on unheated quartz substrates agree with model predictions of contact radius, contact angle, and droplet volume. Model results indicating temperature and velocity distribution across an evaporating water droplet show that the lowest temperatures are at the liquid-gas interface, and a single vortex exists for the predominant duration of the droplet's lifetime. The temperature of the unheated substrate is also significantly reduced due to evaporative cooling. The interfacial evaporation flux distribution, which depends on heat transfer across the droplet and advection in the surrounding medium, shows the highest values near the three-phase contact line. In addition, the model also predicts evaporation dynamics when the substrate is heated and exposed to different advection conditions. Generally, higher evaporation rates result from higher substrate heating and advection rates. However, substrate heating and advection in the surrounding gas have minimal effects on the relative durations of CCR and CCA modes for a given receding contact angle. Specifically, in this case, a 40× increase in substrate heating rate or 7.5× increase in gas velocity can only change these relative durations by 3%. This study also highlights the importance of surface wettability, which affects evaporation dynamics for all the conditions explored by the numerical model.

**Keywords**: Droplet Evaporation, Evaporation Dynamics, Wettability, Sessile Droplet, Marangoni Convection, Thermocapillary Phenomenon

#### **Nomenclature**

$r,z$ $r_q$	cylindrical coordinates, m the radius of the QCM, m
$r_e$	the radius of the electrode, m
$h_d$	droplet height, m
$r_d$	droplet radius, m
$V_{in}$	velocity at the inlet, m/s
h	heat transfer coefficient, W/(m <sup>2</sup> ·K)

velocity, m/s u pressure, Pa p heat capacity at constant pressure, J/(kg·K)  $C_p$ I identity matrix gravitational acceleration, m/s<sup>2</sup> g T temperature, K t time, s k thermal conductivity, W/(m·K) the concentration of water vapor, mol/m<sup>3</sup> С D diffusion coefficient of vapor, m<sup>2</sup>/s  $M_f$ mass flux normal to the interface,  $kg/(m^2 \cdot s)$ the molecular weight of water, kg/mol  $M_w$ R universal gas constant, J/(mol·K) interface heat sink due to evaporative cooling, W/m<sup>2</sup>  $q_e^{"}$ latent heat of vaporization, J/mol  $H_{vap}$ convective heat transfer flux, W/m<sup>2</sup> q" ReReynolds number, 1

# Greek symbols

 $\theta$  contact angle,  $^{\rm o}$  density, kg/m<sup>3</sup>

 $\mu$  dynamic viscosity, Pa·s surface tension, N/m

 $\kappa$  the curvature of the droplet, 1/m

 $\tau$  stress tensor, N/m<sup>2</sup>

#### **Subscripts**

amb ambient condition

*i* interface

*l, g* liquid, gas domain

mesh mesh

0 initial condition at t=0 s

sat saturated

#### 1. Introduction

Evaporation of sessile droplets is a universal phenomenon essential in nature and various industries, with applications spanning DNA chip manufacturing [1], electronic cooling [2-4], inkjet printing [5], semiconductor device manufacturing [6], and microfluidic control [7]. Understanding the factors governing droplet evaporation is crucial for improving the performance of many applications. The three modes of droplet evaporation reported in the literature include the constant contact radius (CCR), the constant contact angle (CCA), and the mixed (CCR and CCA) modes of evaporation [8]. In the CCR mode, the droplet is pinned on the substrate surface resulting in a constant radius and a decreasing contact angle, while in the CCA mode, the contact angle is constant, and the contact radius decreases. In the mixed mode, both contact radius and angle can

diminish. A common variation of these modes in stick-slip droplet motion is also observed, where the CCA and CCR modes occur in tandem [9, 10]. The CCR, CCA, and mixed modes typically occur sequentially for sessile droplet evaporation on flat surfaces.

Modeling single droplet evaporation represents a multiphysics problem involving coupled heat transfer in three phases, evaporative cooling effect, Marangoni flow in the droplet, and vapor transport in the gas domain [11]. It is challenging to account for all these mechanisms analytically; therefore, some simplifications exist in prior theoretical efforts. One of the classic theories for sessile droplet evaporation was developed by Picknett and Bexon [12], in which the droplet is a spherical cap, and the evaporation occurs only through diffusion. In this case, heat transfer and fluid flow were omitted; consequently, the model, although helpful, has limited validity. Building on Picknett and Bexon's classic diffusion theory, Sefiane and Bennacer incorporated thermal diffusion in the liquid droplets and the substrate with the addition of the evaporative cooling effect, which improved the applicability of the original model [13].

In diffusion-based models, the omission of convection in the surrounding gas [14, 15] and Marangoni flow [16, 17] inside the droplet can cause significant deviation from experimentally observed evaporation kinetics. Here, numerical simulations complement theoretical models and experiments by accounting for these physical mechanisms and providing a detailed picture of the evaporation process. A typical numerical strategy is to utilize a quasi-steady model by assuming a fixed droplet shape [18-20]. For example, Hu and Larson used this approach to study evaporation with the finite element method by assuming a diffusion-driven process and obtained good agreement with the classic diffusion theory and experiments [18]. However, besides the limited applicability of diffusion-based quasi-steady models, since the droplet profile varies due to mass loss during evaporation, it may not accurately capture the transport characteristics.

Two approaches are often used to address the evolving droplet shape. One involves decoupling the physics with the droplet's rapid shape evolution. In this case, the transient evaporation process is divided into several time steps that are quasi-steady with a fixed droplet shape. The droplet shape in each time step is obtained using the spherical cap assumption and by relating the droplet volume and the average evaporation rate in the previous time step [21-24]. The other approach simulates the moving interface, coupling the physics with droplet evolution, which gives better accuracy [25]. Here, the interface capturing and tracking methods predict the droplet shape. Interface capturing methods include the lubrication theory [26], the level set (LS) [27], the phase field [28], and the volume of fluid (VOF) methods [29, 30], in which a dedicated function reconstructs the interface shape and the computational mesh is fixed. The interface tracking methods, on the other hand, track the moving interface with a deforming mesh due to the movement of the interface. Front tracking [31], immersed boundary [32], and arbitrary Lagrangian-Eulerian (ALE) methods [33-36] are some of the interface tracking methods.

Recent interface capturing and tracking methods have complemented our understanding of droplet evaporation from prior quasi-steady models. For example, Murisic and Kondic considered spontaneous evaporation of water and isopropanol on smooth silicon substrates without contact line pinning. The theoretical model includes thermocapillary and heat diffusion effects and determines evaporation flux based on two approaches wherein evaporation is assumed transport

limited either in the vapor or the liquid phase. The study discusses how modeling can predict which of the two approaches is suitable for a given experiment [26]. Muramatsu et al. used the LS method to investigate the evaporation of a pendent bi-component droplet surrounded by air [37]. They studied the influence of initial composition and ambient temperature on the evaporation characteristics of a bi-component fuel droplet. Since a constant surface tension was assumed, the temperature and solute dependence of surface forces was not considered. Shang et al. developed a VOF approach to simulate the evaporation of both suspended and sessile droplets [25]. They studied the effect of ambient humidity on evaporation dynamics of sessile drop under CCA mode. They used a constant surface tension ignoring its temperature dependence. Sáenz et al. studied the evaporation of non-axisymmetric drops using experiments and three-dimensional direct numerical simulations. In this study, non-circular drops show variable wettability along the contact line, which is sensitive to the choice of system parameters and inversely dependent on the local contactline curvature. The study demonstrates that the average interface temperature remains relatively constant during evaporation in the constant contact angle mode while it increases in the constant contact radius mode [38]. Yang et al. developed a transient sessile droplet evaporation model using the ALE method [33]. While the model considered the relevant physics for sessile droplet evaporation, including temperature-dependent surface tension, convective mass transfer in ambient air was omitted, and the simulation considered only the CCR evaporation mode. Subsequently, Chen et al. improved the ALE model to investigate the influence of the initial contact angle, liquid volatility, and substrate properties on evaporation [34, 36]. This ALE model included the effect of natural convection on evaporative mass flux.

Prior studies indicate simulation of either CCA or CCR modes of evaporation, omission of the temperature dependence of surface tension, and convective mass transfer. Consequently, only a few studies have reproduced experimentally-observed CCR, CCA, and mixed modes. These efforts use the Lattice Boltzmann approach on the mesoscale [39] and the molecular dynamics method on the microscale [40]. Doursat et al. numerically studied macroscale droplet evaporation on a substrate under forced flow [41]. While a continuous variation in the CCR and CCA modes was studied, this model considered only the droplet and the substrate, and diffusion heat transfer. Besides, the droplet shape was calculated based on the spherical cap assumption with a known volume. Therefore, a comprehensive macroscale model is necessary to simulate the CCR and CCA modes in sequence, considering both the thermocapillary (Marangoni) flow and the convective mass transfer, without using the spherical cap assumption.

This study uses a two-step ALE moving mesh model to simulate the CCR and CCA modes of sessile droplet evaporation. The ALE method not only tracks the sharp liquid-gas interface but obviates the need for the spherical cap assumption. Since the interfacial force balance determines the droplet shape, the model can handle deviations from a spherical shape, especially near the three-phase contact line [42, 43]. This model solves vapor transport in the gas phase, flow in the liquid and gas phases, and heat transfer across all three phases. In addition, the Marangoni flow due to surface tension gradient and the convective mass flux due to ambient gas flow is incorporated in this model. The model is validated using experiments and data from independently conducted tests. The study complements experiments by probing the velocity field of the droplet,

the temperature distribution of the droplet and the substrate, and the local mass flux at the liquidgas interface that is not readily available from experiments. In addition, this study explores the effect of substrate heating and ambient flow conditions, giving additional insight into sessile droplet evaporation dynamics – an essential step towards leveraging this mechanism in applications ranging from thermal management of electronics to self-assembly-based fabrication.

#### 2. Methods

The simulation conducted in this paper analyzes droplet evaporation on a quartz substrate. While the experimental setup has been described in detail in prior publications [24, 44], a brief description of the testbed is provided below, followed by the numerical model.

# 2.1. Experimental Setup

Experiments were performed inside an enclosure maintained at room temperature, as shown schematically in Figure 1(a). Low-speed nitrogen flow (99.999% N<sub>2</sub>, Airgas) maintained a constant relative humidity (0-2%) inside the 45 × 45 × 300 mm enclosure. The evaporation rate was quantified using a quartz crystal microbalance (QCM) as a droplet radius sensor and a goniometer as a contact angle sensor. Figure 1(b) illustrates the top and cross-sectional views of an evaporating droplet on the QCM. The sessile droplets evaporate on planar 10 MHz AT-cut QCM crystals with polished surfaces and keyhole-shaped gold electrodes. The average roughness of the crystal surface is close to 50 Å. Under these conditions, the QCM's response to changes in droplet contact radius is given by the following [44].

$$\Delta f = -f_o^{3/2} \sqrt{\frac{\rho \mu}{\pi \rho_q \mu_q}} \left( 1 - e^{-2ar^2/r_e^2} \right) \tag{1}$$

Here,  $\Delta f$  is the change in the resonance frequency,  $\Delta f = f - f_0$ , where f is the resonant frequency,  $f_0$  is the unloaded resonant frequency,  $\rho$  is the fluid density,  $\mu$  is the fluid viscosity,  $\rho_q$  is the quartz density, and  $\mu_q$  is the quartz shear modulus. Equation (1) describes the frequency shift based on a droplet's finite contact radius, r, on a QCM with electrode radius  $r_e$ . Here, the constant a is intrinsic to the QCM, which has a value of unity for the type of QCM used in this work [45-48]. Note that the equation above does not indicate any contact angle dependence. As found in our previous work, the contact angle is relevant only for microscopically-tiny droplets [47].

Unlike the droplet radius, r, obtained using the QCM response (Equation (1)), the droplet contact angle,  $\theta$  was measured using a goniometer (Ramé-Hart). The goniometer, consisting of a light source and a camera, determines the contact angle by finding the liquid-vapor interface and locating the regions corresponding to the maximum change in light intensity or image contrast. The interface is then fit to a circular profile by a least-squares curve fit, and the contact angle is found by numerical differentiation at the three-phase contact point. The droplet height and volume are obtained from  $\theta$  and r assuming a spherical cap shape and calculated as  $h = r \tan(\theta/2)$  and  $V = \pi(3r^2h + h^3)/6$ , respectively. The capillary length is given by  $\kappa^{-1} = \sqrt{\gamma/\rho g}$ , where  $\gamma$  is the surface tension, and g is the acceleration due to gravity. All droplets examined in this work have dimensions smaller than the capillary length, approximately 2.7 mm for water for these conditions. Hence, the spherical cap assumption is suitable for calculating h and V. In the

experiments, the evaporation rate is determined by taking the time derivative of the volume. In order to minimize the noise in the calculated derivative of the droplet volume, a piecewise linear fit was applied to the raw volume data to determine the evaporation rate.

All experiments followed a standard cleaning protocol for the QCM crystals involving sonication in isopropanol and de-ionized water baths. The experiments were conducted by placing the OCM inside an enclosure maintained at the desired temperature and moisture, as illustrated in Figure 1. The enclosure enabled nitrogen gas flow at low speeds to displace moist air surrounding the droplet. Hence, the humidity in the enclosure was held constant at 0 to 2%. Temperature measurements of the nitrogen stream indicated a steady value during experiments. Measurements were acquired using humidity (Honeywell HIH-4000) and temperature sensors (J-Type thermocouples). A manual syringe with a 22-gauge needle was used to deposit droplets on the QCM surface. The initial contact angle of each case was obtained soon after the droplet was deposited on the QCM surface, and the receding contact angles correspond to the angle measured when the droplets de-pin from the surface. Data acquisition of temperature, humidity, and frequency began several minutes before droplet deposition and continued for 60 seconds after the droplet had evaporated entirely. Contact angle measurements began when the droplet was deposited and continued at a measurement rate of one per second until the droplet was no longer visible. The experimental measurements were performed identically to those described in more detail in the reference [24].

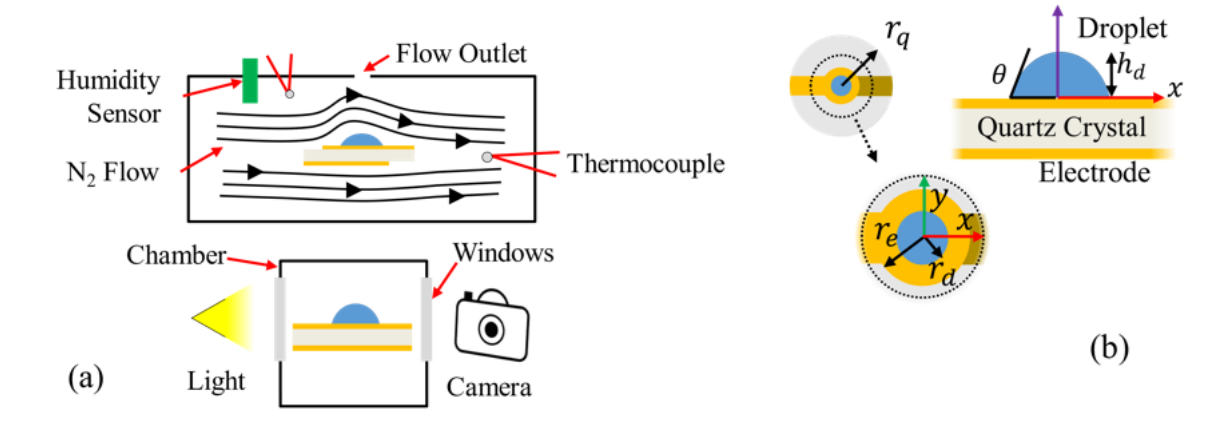


Figure 1. (a) Schematic of the experimental setup with a side view (top) showing pure nitrogen flow, humidity, and temperature sensors inside the chamber. The front view (bottom) illustrates using a light source and a camera to record the droplet geometry. (b) The top and cross-sectional illustrations of an evaporating droplet on a quartz crystal microbalance. Here,  $r_q$ ,  $r_e$ , and  $r_d$  are the radius of the quartz crystal, the electrode, and the droplet, respectively.  $\theta$  is the contact angle, and  $h_d$  is the droplet height.

#### 2.2. Numerical Model

Sessile droplet evaporating on any substrate involves complex physical processes, including mass transfer, fluid flow, and heat transfer, while the droplet shape changes due to evaporation into the surrounding gas. Therefore, the ALE moving mesh model was developed to accurately

simulate the physical phenomena and track the sharp liquid-gas interface. The physical description, governing equations, and numerical procedures are described below.

### 2.2.1 Physical Description

Figure 2 illustrates the two-dimensional (2D) axisymmetric computational domain and the boundary conditions used in the model. The overall domain is a rectangle of width 50 times the initial contact radius (50  $r_{d,0}$ ) and a height of 25  $r_{d,0}$ . The water droplet sits in the center of the quartz substrate, surrounded by nitrogen gas. The gas inlet is at the center of the computational domain, and the outlet is the right-side boundary, as indicated in Figure 2. Different wall conditions are applied at the substrate-droplet interface to simulate the two evaporation modes (CCR, CCA). A no-slip wall condition was used for the CCR mode, while a Navier slip condition was used for the CCA mode. The gas flow from the inlet generates a radially outwards decelerating flow in the chamber.

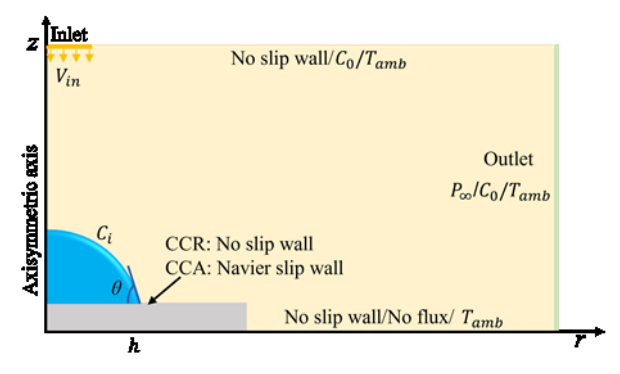


Figure 2. The computational domain consists of a droplet centrally placed on a quartz substrate surrounded by nitrogen gas  $(N_2)$ . The boundary conditions for constant contact radius (CCR) and constant contact angle (CCA) evaporation modes utilize no-slip, and Navier slip conditions, respectively. As shown above, other boundaries include the axisymmetric, wall, and outlet conditions.

#### 2.2.2. Governing Equations

The gas domain physics is governed by mass continuity, momentum balance, conservation of energy, and vapor transport equations, as listed below.

$$\nabla \cdot \mathbf{u} = 0 \tag{2}$$

$$\rho \frac{\partial \mathbf{u}}{\partial t} + \rho (\mathbf{u} \cdot \nabla) \mathbf{u} = \nabla \cdot [-p\mathbf{I} + \mu (\nabla \mathbf{u} + (\nabla \mathbf{u})^{\mathsf{T}})] + \rho \mathbf{g}$$
(3)

$$\rho C_p \frac{\partial T}{\partial t} + \rho C_p \mathbf{u} \cdot \nabla T + \nabla \cdot (-k \nabla T) = 0$$
(4)

$$\frac{\partial c}{\partial t} + \mathbf{u} \cdot \nabla c = \nabla (D \nabla c) \tag{5}$$

Here  $\rho$  is the density, **u** is the velocity vector,  $\mu$  is the dynamic viscosity,  $C_p$  is the heat capacity at constant pressure, T is temperature, k is the thermal conductivity, c is the concentration of water vapor, and D is the diffusion coefficient of vapor in nitrogen.

In the droplet (liquid), the flow and heat transfer is governed by the continuity, momentum balance, and energy conservation equations that are of the same form as the gas domain except for the thermodynamic properties. Only heat conduction is considered in the solid domain, which reduces the energy conservation equation to the following.

$$\rho C_p \frac{\partial T}{\partial t} + \nabla \cdot (-k\nabla T) = 0 \tag{6}$$

#### 2.2.3. Initial and Boundary Conditions

In the liquid and gas domains, the initial velocity is zero. While the initial pressure in the gas domain is 1 atm, the initial pressure in the liquid domain is 1 atm adjusted by the Laplace pressure  $\Delta p$ , shown below,

$$\Delta p = 2\sigma_0 \kappa_0 \tag{7}$$

where  $\sigma_0$  is the initial surface tension, and  $\kappa_0$  is the initial curvature of the droplet.

The initial temperature in the entire computational domain is set as the ambient temperature measured in the experiments. In addition, the initial vapor concentration is set to the ambient vapor concentration from relative humidity measurements in the experiments, which is zero.

In order to capture the droplet shape evolution due to evaporative mass loss and surface tension variation, an interfacial force balance is considered at the liquid-gas interface. The surface tension,  $\sigma$  is given by the following equation where temperature, T is in Kelvin scale.

$$\sigma = 0.0728 - 0.0001688(T - 293.15) \tag{8}$$

The normal and tangential force balance equations at the liquid-gas interface are given by:

$$\mathbf{n}_i \cdot (\tau_a - \tau_l) = \sigma(\nabla_s \cdot \mathbf{n}_i) \mathbf{n}_i - \nabla_s \sigma \tag{9}$$

$$\nabla_{s} = (\mathbf{I} - \mathbf{n}_{i} \mathbf{n}_{i}^{T}) \nabla \tag{10}$$

$$\tau = -p\mathbf{I} + \mu(\nabla \mathbf{u} + (\nabla \mathbf{u})^{\mathsf{T}}) \tag{11}$$

where  $\mathbf{n}_i$  is the interfacial normal pointing outside the droplet,  $\tau$  is the total stress tensor and  $\nabla_s$  is the surface gradient operator. The subscripts g and l denote the gas and liquid domain, respectively.

In the ALE modeling approach, the mesh velocity at the interface is defined by the following equation,

$$\mathbf{u}_{mesh} = \left(\mathbf{u}_l \cdot \mathbf{n}_i - \frac{M_f}{\rho_l}\right) \mathbf{n}_i \tag{12}$$

$$M_f = M_w((-D\nabla c + \mathbf{u}c) \cdot \mathbf{n}_i)$$
(13)

where  $M_f$  is the magnitude of mass flux normal to the interface,  $M_w$  is the molecular weight of water. The velocity of the contact line in CCA mode is evaluated using the Navier slip boundary condition, which enforces no-penetration at the wall and adds tangential stress, given by the following equations:

$$\mathbf{K}_{nt} = \frac{\mu}{\beta} \mathbf{u}_{slip} \tag{14}$$

$$\mathbf{K}_{\mathrm{nt}} = \mathbf{K}_{\mathrm{n}} - (\mathbf{K}_{\mathrm{n}} \cdot \mathbf{n}_{\mathrm{wall}}) \mathbf{n}_{\mathrm{wall}}, \mathbf{K}_{\mathrm{n}} = \mathbf{K} \mathbf{n}_{\mathrm{wall}}$$
 (15)

$$\mathbf{u}_{\text{slip}} = \mathbf{u} - (\mathbf{u} \cdot \mathbf{n}_{\text{wall}}) \mathbf{n}_{\text{wall}} \tag{16}$$

$$\beta = f_{\rm h} h_{\rm min} \tag{17}$$

Here,  $\mathbf{K}_{nt}$  is the tangential stress tensor,  $\mathbf{K}$  is the viscous stress tensor,  $\mathbf{u}_{\text{slip}}$  is the velocity tangential to the wall,  $\mu$  is the viscosity,  $\beta$  is the slip length,  $h_{min}$  is the smallest element side, which in this case is  $1.78 \times 10^{-5}$  m, and  $f_{\rm h}$  is a factor of minimum element length, wherein  $f_{\rm h} = 0.5$  was used in the current model.

The vapor concentration at the liquid-gas interface is given by  $c_i = p_{sat}/RT$ , where saturation pressure,  $p_{sat}$  is calculated as a function of temperature using the following equation [49].

$$p_{sat} = \frac{\exp\left(77.3450 + 0.0057T - \frac{7235}{T}\right)}{(T)^{8.2}} \tag{18}$$

In order to account for evaporative cooling, a boundary heat sink  $q_e^*$  is applied at the liquid-gas interface, given by  $q_e^* = -M_f H_{vap}$ , where  $H_{vap}$  is the latent heat of vaporization. Besides, the base of the gas domain is assigned a zero vapor flux, and the vapor concentrations along the side and top boundaries of the gas domain are maintained at the ambient vapor concentration, which is zero.

A velocity inlet at the top center and an outlet along the side of the computational domain are assigned for flow analysis. Other boundary conditions for flow analysis include the no-slip condition along the walls, as shown in Figure 2. All the boundaries for heat transfer analysis are set at the ambient temperature except the boundary underneath the substrate heat transfer, q'' takes place via natural convection,

$$q'' = h \cdot (T_{\text{amh}} - T) \tag{19}$$

where h is the heat transfer coefficient with a value of 8.4 W/m<sup>2</sup>K for these conditions [50].

#### 2.2.4. Numerical Procedure

The axisymmetric model is built and solved using Comsol Multiphysics 5.6 – a commercial solver for finite element analysis. The ALE moving mesh applied in the model enables tracking of the sharp liquid-gas interface. The deformation domains are the fluid-occupied regions - the gas and liquid domains. Since the mesh deforms due to evaporation in the fluid region, the computational domain is re-meshed automatically when a low mesh quality is encountered. For the sake of simulating the two-step evaporation process starting with CCR followed by CCA mode, the solution of the last time step of CCR mode is set as the initial value for the CCA mode to analyze continuous evaporation. The transition from CCR to CCA mode occurs when the contact angle corresponds to the receding contact angle – a parameter that depends on the substrate and the liquid, which can be quantified using experiments.

In this finite element study, a quadratic Lagrange shape function is utilized, which reduces the degrees of freedom by using isoparametric elements. Besides, the second-order shape function is more accurate than its linear counterpart. Furthermore, the three-phase contact line of the droplet can be a sharp corner at low contact angles, which can give rise to numerical errors during

automatic re-mesh. In order to avoid these errors, the CCR mode is divided into two sub-steps. The first sub-step allows the contact angle to decrease to 30°. Using the final time step as the initial value for the second sub-step of the CCR mode, the contact angle is allowed to reach the receding contact angle. In the second sub-step of CCR mode, the velocity shape function is cubic to facilitate higher accuracy. The relative tolerance for all variables for convergence was set as 0.001, and a mesh-dependence study was carried out to eliminate the influence of mesh. Specifically, the mesh size near the droplet was one-twentieth of the initial contact radius. The relative differences in contact radius, contact angle, and droplet volume between this mesh and a finer mesh were less than 2%.

#### 3. Results

We first discuss model validation by comparing results with experiments conducted in the lab and independent data published in the literature. Then, the droplet and substrate temperature distribution, the velocity field inside the droplet, and the interfacial mass flux are discussed for a specific operating condition. Finally, the influence of substrate heat flux and inlet velocity on the evaporative dynamics of the droplet is investigated.

#### 3.1. Model Validation

The model simulates the same conditions encountered in the experiments listed in Table 1. For these six droplets, the volume, the initial contact angle, initial contact radius, receding contact angle, ambient temperature, and the inlet velocity for the model are taken from the experimental data. The ambient relative humidity in all the experiments was maintained close to 0% using dry nitrogen gas.

Experiments	Case A	Case B	Case C	Case D	Case E	Case F
Initial volume (mm <sup>3</sup> )	2.79	3.14	4.05	2.04	2.85	4.37
Initial contact angle (°)	69.41	66.29	72.18	59.21	66.22	66.40
Initial contact radius (mm)	1.30	1.39	1.44	1.27	1.35	1.55
Receding contact angle (°)	18.39	17.56	18.77	15.73	15.64	13.66
Ambient temperature (K)	298.36	298.28	297.46	297.18	297.34	296.71
Inlet velocity (m/s)	0.35	0.35	0.40	0.40	0.40	0.40

Table 1 Simulation cases – model inputs in the current study

Table 1 shows variations in the initial and receding contact angles for cases A to F. Although the experiments used the same quartz crystal for all the cases, several factors can contribute to different initial and receding contact angles. The random roughness on the QCM surface, the variation in surface energy caused by slight differences in cleaning, handling, and environmental factors, and the non-volatile impurities in the liquid, also detected by the QCM, can lead to differences in the initial and receding contact angles in cases A to F.

Figures 3 and 4 compare the computed droplet contact radius, contact angle, droplet volume, and droplet height with experiments. The error bands associated with the measurement of contact angle and radius shown in Figure 3 result in the uncertainties associated with the droplet height and volume shown in Figure 4. Transitioning between CCR and CCA, there is an obvious plateauing of contact angle in cases B, D, and E once the droplets start receding; therefore, the receding contact angles are set to these plateauing values. However, in cases A, C, and D, the contact angle continuously decreases during evaporation; hence, the receding contact angles are set to the values when the contact radius exhibits an apparent receding behavior.

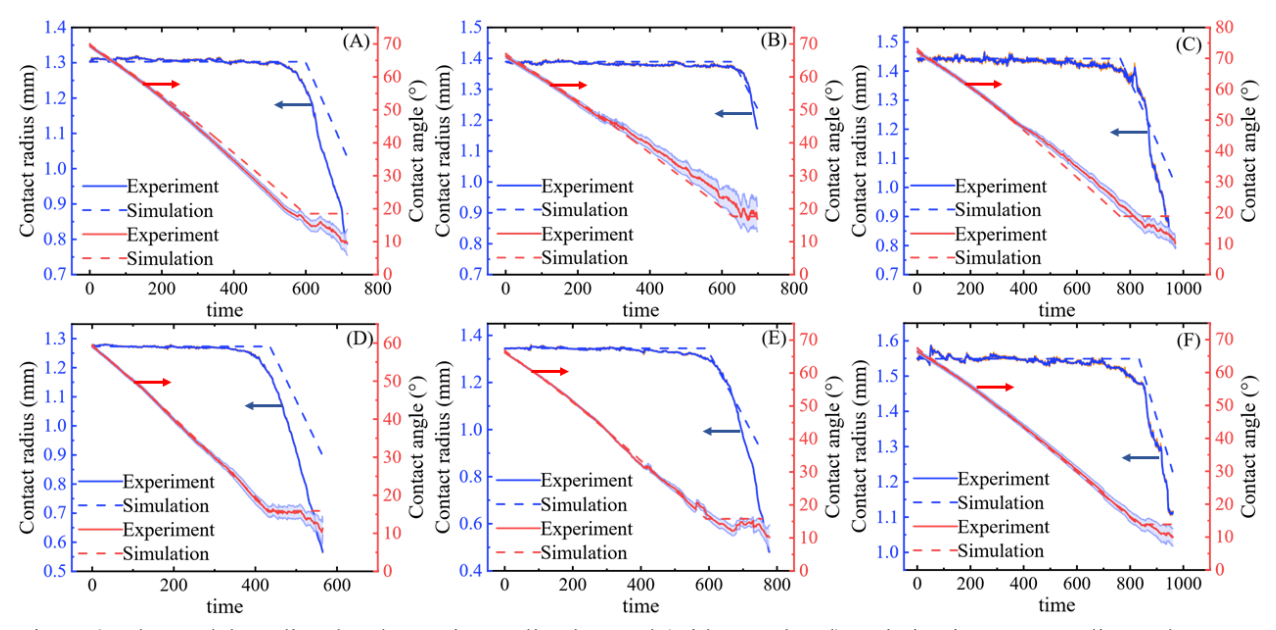
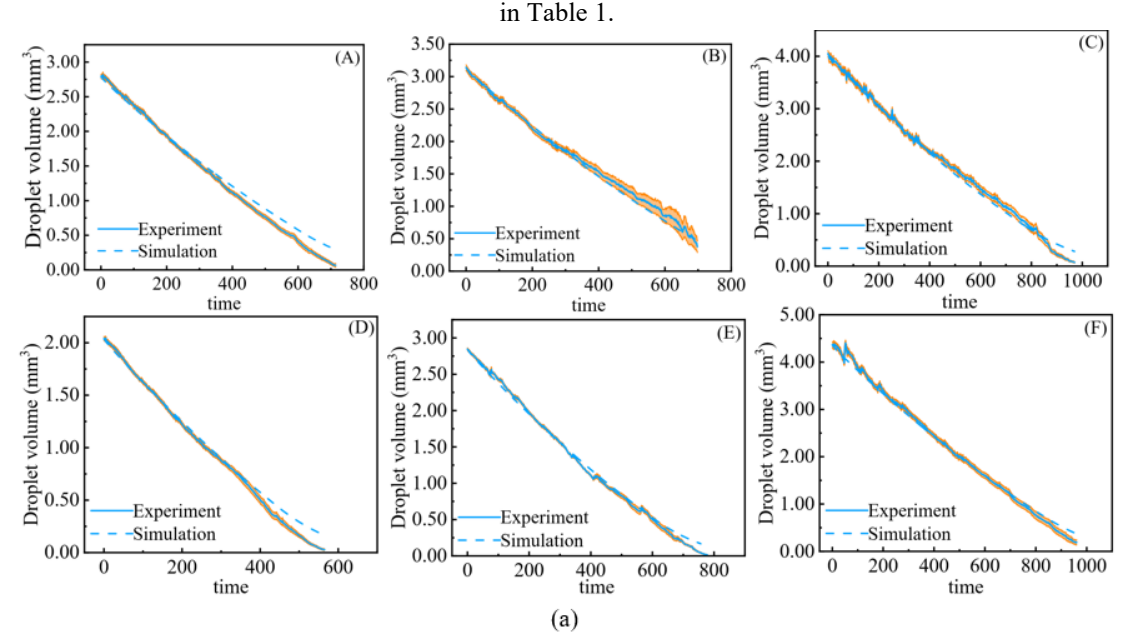


Figure 3. The model predicted and experimentally observed (with error band) variation in contact radius and contact angle during droplet evaporation across multiple experiments – cases (A) to (F) correspond to the conditions listed



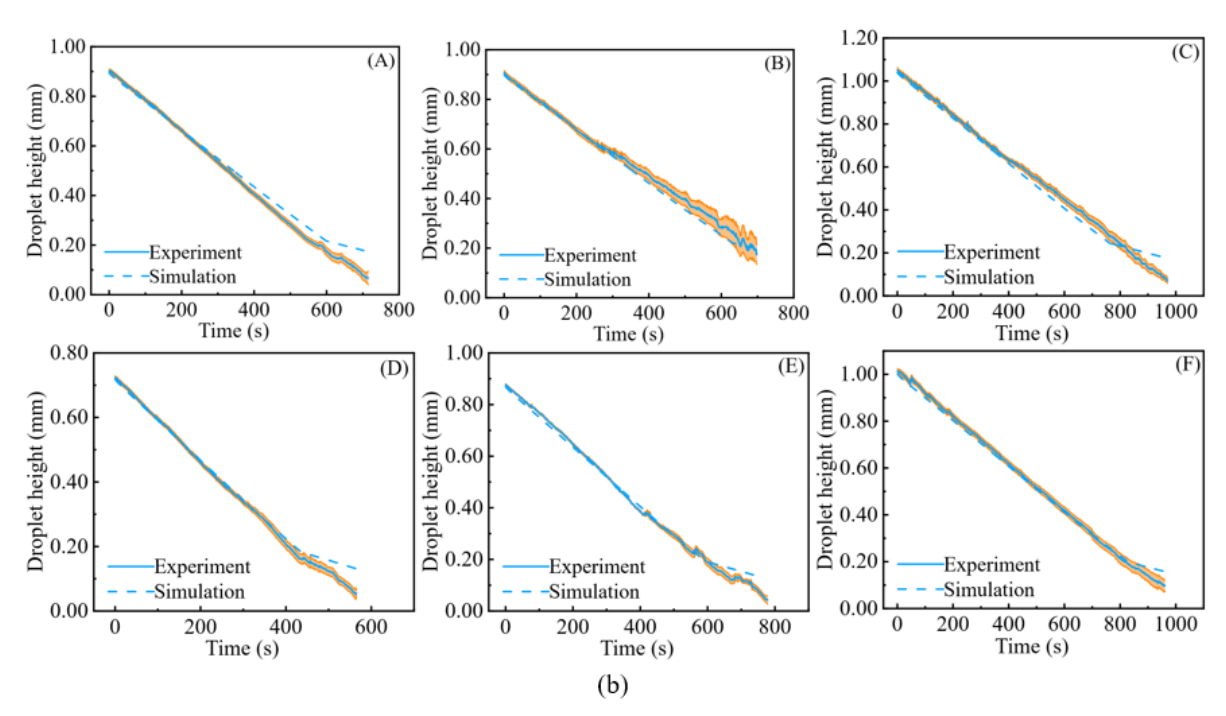


Figure 4. (a) The variation in droplet volume versus time seen in experiments and model predictions. (b) The change in droplet height versus time comparing model predictions and experiments. The error bands indicate uncertainties in droplet volume and height. Here again, cases (A)-(F) correspond to the conditions listed in Table 1.

A comparison of experiments and model predictions shows that the CCR and CCA evaporation modes are successfully predicted by the ALE moving mesh model. The model-predicted variation in the contact angles, contact radii, droplet volumes, and droplet heights in the six cases agree well with the experiments. Slight discrepancies occur when the contact radius and angle simultaneously decrease when evaporation is not strictly in the CCR or the CCA mode. Hence, for this period of simultaneous change, the model fails to capture the gradual decrease in radius seen in experiments during the transition from CCR to CCA modes. Also, the simulation does not consider evaporation in the mixed mode occurring at the experiment's final stages, which accounts only for a small fraction of the total droplet lifetime in this study. Generally, this two-step ALE moving mesh model simulates the CCR and CCA modes in sequence and accurately predicts droplet evaporation and shape evolution.

The model is also compared with independent experiments conducted by Belmiloud et al. consisting of an ultra-pure water droplet evaporating on a silicon substrate surrounded by still air [6]. Here, the initial contact angle and contact radius are 64° and 1.28 mm, respectively. The CCR to CCA transition happens when the contact angle reaches 34°. In order to simulate this experiment, the vapor transport took place in a diffusive environment, and the boundary conditions for the surrounding air were set as open boundaries since there were no inlets or outlets. Figure 5 shows the model-predicted and experimentally observed contact radius (blue) and angle (red), showing excellent agreement. The relative difference in contact angle measured in Belmiloud et al.'s experiment and model predictions in this study is within 5%. Similarly, the relative difference in measured and model-predicted contact radius is no more than 5% for most of the experiment except for the last few seconds of the droplet lifetime. The relative difference at the end of the

evaporation process is 7% to 11%, possibly due to measurement errors associated with relatively tiny droplets. The model generally agrees with experiments for this two-step evaporation process, demonstrating the capability to simulate droplet shape evolution and evaporative dynamics.

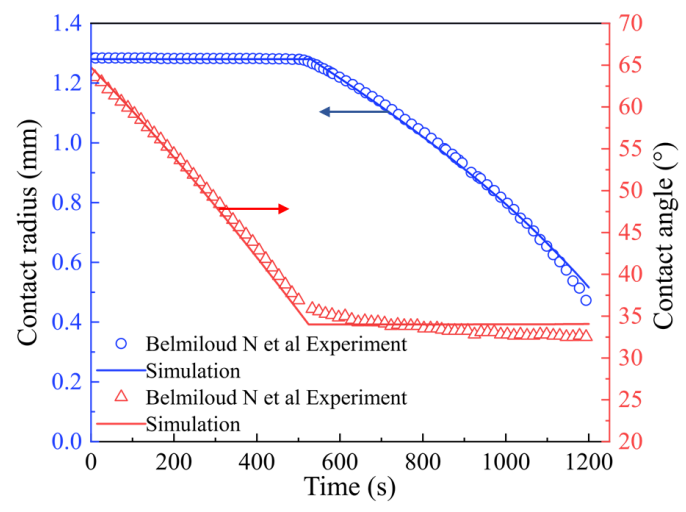


Figure 5. A comparison of model-predicted contact radius and contact angle with independent experiments conducted by Belmiloud et al. [6].

# 3.2. Temperature and Velocity Distribution

We picked case D (arbitrarily) to study the temperature distribution, the velocity field, and interfacial mass flux where both CCR and CCA modes are observed. While there is an apparent quantifiable change in droplet shape seen in experiments, the temperature distribution and velocity fields that control evaporation dynamics are often challenging to measure, but these parameters can be investigated in detail via numerical modeling.

Figure 6 shows the temperature of the droplet and the substrate at different times. Three stages of evaporation are displayed in the three rows of Figure 6: (1) the early stages of the CCR mode, (2) the middle of the CCR mode, and (3) the early stages of the CCA mode. In this case, the transition from the CCR to the CCA mode occurs at around 430 seconds. Initially, the substrate and droplet temperatures are uniform, close to the ambient temperature of 297 K. After a second, while the substrate is close to the ambient temperature, a slight drop can be seen in the droplet due to the evaporative cooling effect. Subsequently, the evaporative cooling effect spreads through the droplet and substrate. The cooling effect becomes more evident in the later stages of CCR and CCA modes with a significant reduction in the temperature, especially within and in the vicinity of the droplet, as shown in the second and third rows in Figure 6.

The radial temperature gradient seen in the substrate is nearly constant during most of the CCR and CCA modes. The temperature at the outer boundaries of the substrate remains invariant since the rate of heat loss from evaporation and the substrate (quartz) conductivity are both relatively low to cause any effect on the substrate temperature far from the droplet.

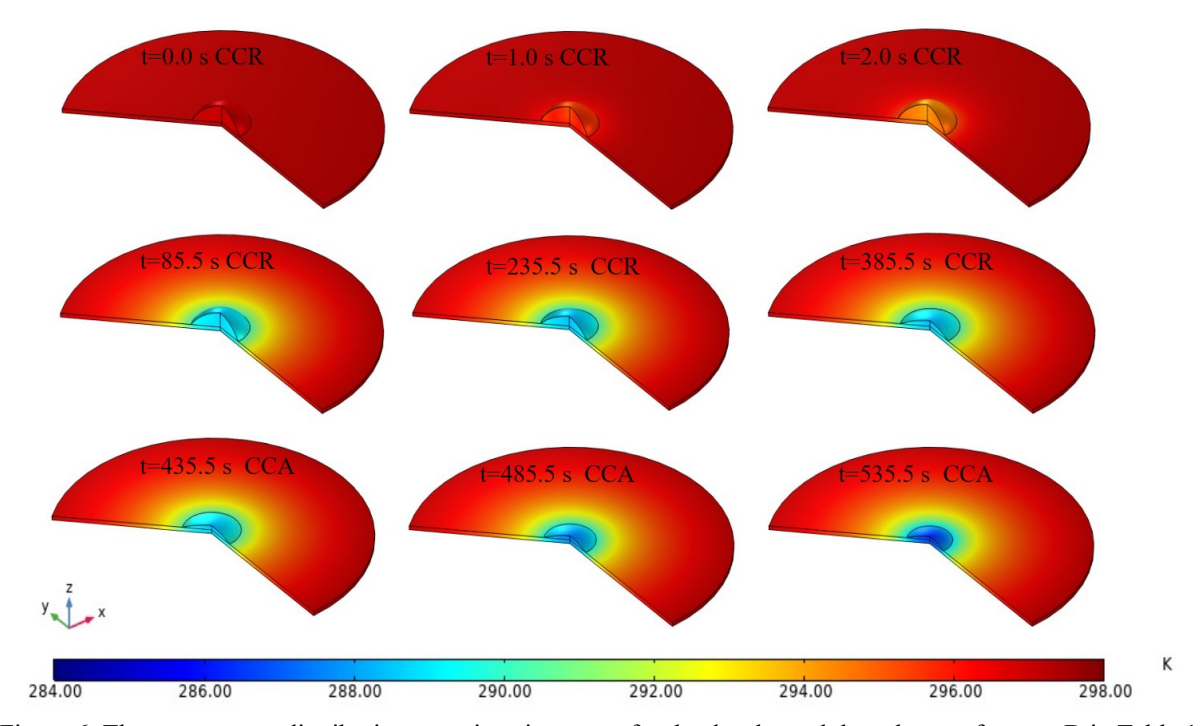


Figure 6. The temperature distribution at various instances for the droplet and the substrate for case D in Table 1.

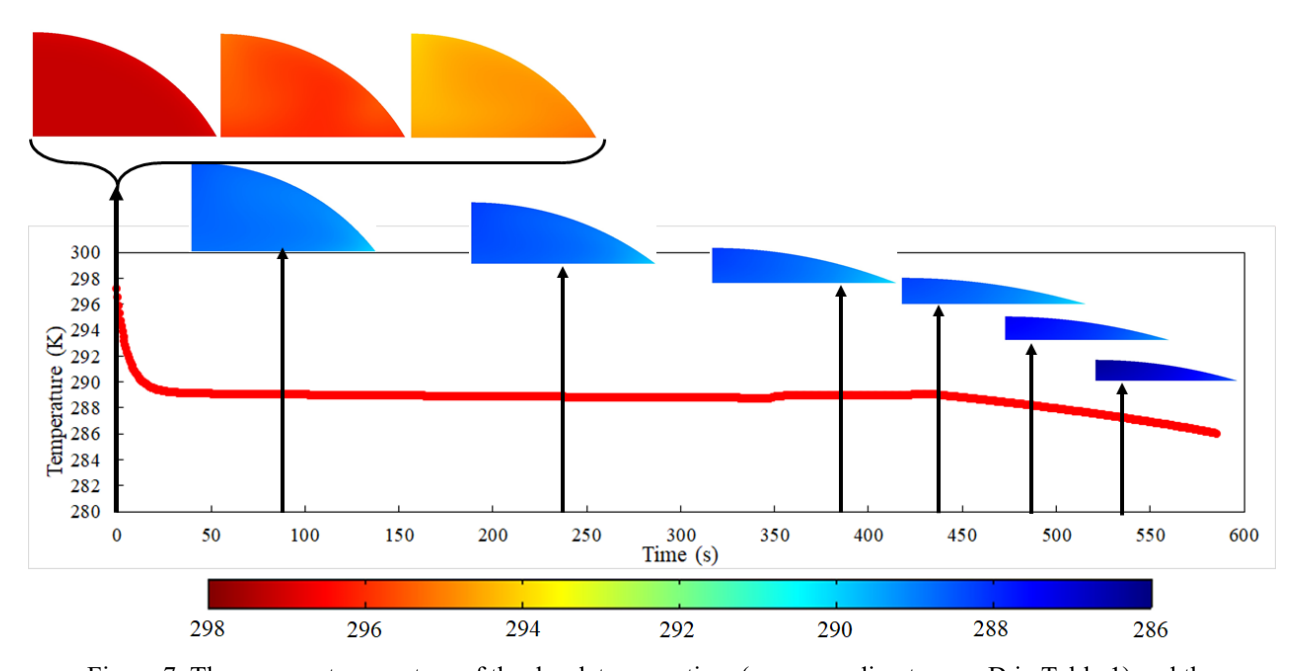


Figure 7. The average temperature of the droplet versus time (corresponding to case D in Table 1) and the temperature distribution across the droplet at various instances.

Figure 7 shows the variation in the average temperature, and the insets show the temperature across the droplet corresponding to the same instances as Figure 6. The average temperature of the droplet falls precipitously in the first few seconds due to droplet evaporation into an absolutely dry environment. The subsequent variation in the temperature of the droplet in the CCR mode is

relatively minimal. Minor temperature variations stem from the competing effects of evaporative cooling and droplet heating from the underlying substrate. During this period, the droplet is large enough to have a high thermal conduction resistance. Consequently, the rate of heat loss by evaporation supersedes the heat gained from the substrate, causing the average droplet temperature to decrease. The droplet is flatter in the final stages of the CCR mode, corresponding to a lower thermal conduction resistance across the droplet. Hence, from the start of the CCA mode (around 435 s), the average droplet temperature decreases much faster because of the receding contact area, which lowers the heat transfer rate from the substrate to the droplet. Although not apparent in the insets, the coldest temperatures are at the droplet-gas interface farthest from the substrate, where evaporation results in self-cooling. Near the three-phase contact line, the temperatures are higher and close to substrate temperatures. The heat transfer in this region is quite efficient due to the relatively low liquid film thickness giving rise to higher evaporation fluxes, as discussed in the subsequent sections.

Modeling predictions of these experiments show that the substrate cooling region is roughly 1.7 times the droplet size. This region corresponds to at least a 50% temperature drop ( $T_{\rm amb}-T$ ) relative to the maximum temperature drop seen in the substrate during evaporation, which occurs right underneath the droplet. Hence, a continuous supply of evaporating droplets with a characteristic spacing of roughly 2 × droplet diameter could efficiently dissipate heat from a uniform heat source underneath the quartz substrate. More generally, a similar modeling approach could help design evaporative cooling techniques (e.g., spray cooling) for applications like the thermal management of electronics.

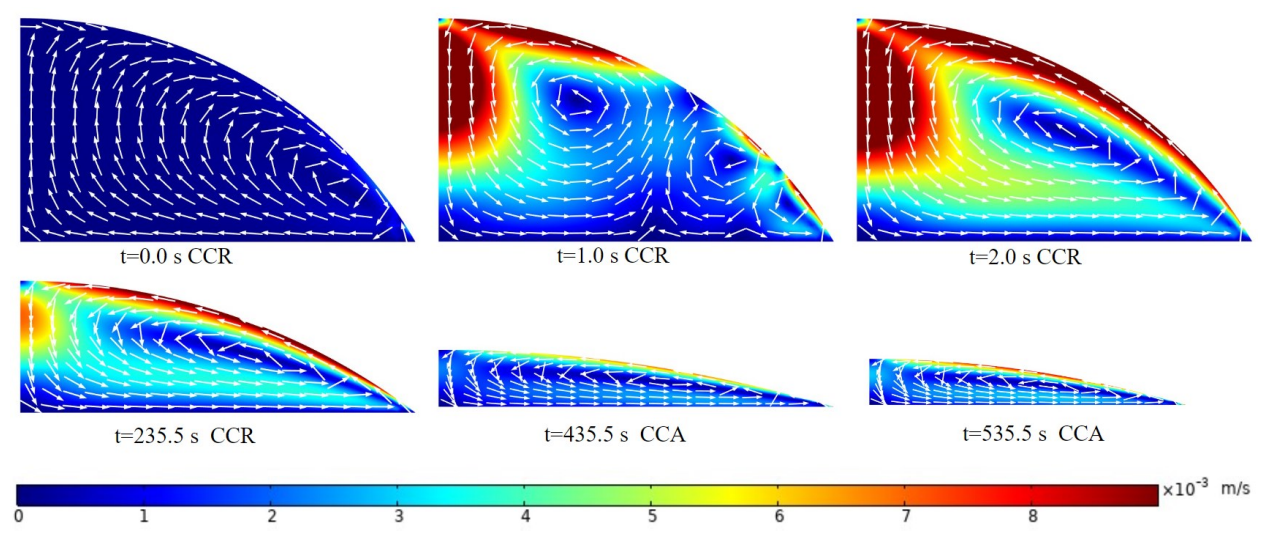


Figure 8. Velocity distribution inside the drop as a function of time (for case D in Table 1). Arrows indicate the flow direction, and the contour (see legend) indicates the velocity magnitude.

Figure 8 shows the velocity magnitude and flow direction across the droplet cross-section in this axisymmetric model at different time points. Initially, the velocity magnitude is negligible due to stagnant conditions assumed as the initial condition of the droplet. Clockwise flow occurs inside the droplet due to the shear stress exerted by the surrounding nitrogen (gas) flow. A second after the start of the evaporation process, three vortices emerge. These three vortices in the droplet are

due to the Marangoni flow caused by the uneven surface tension distribution. In this case, the surface tension dominates the flow since the droplet radius is less than the capillary length, which is around 3 mm for these conditions. Subsequently, only a single counterclockwise vortex survives within the droplet for both CCR and CCA modes. The velocity field inside the droplet under these conditions indicates that water experiences Marangoni flow. This flow could be critical and more severe in many applications, especially those involving volatile liquids. For example, it can influence the deposition pattern if the evaporating droplet is particle-laden. Therefore, the inclusion of Marangoni flow inside the droplet is a crucial component of the analysis.

#### 3.3. Interfacial Mass Flux

The interfacial mass flux and temperature can elucidate aspects of evaporation dynamics that are difficult to observe via experiments. Figure 9 shows the local mass flux along the liquid-gas interface at different times. The x-axis in Figure 9 is the r-coordinate of the liquid-gas interface normalized with the droplet radius – hence, it varies from 0 to 1 at all times.

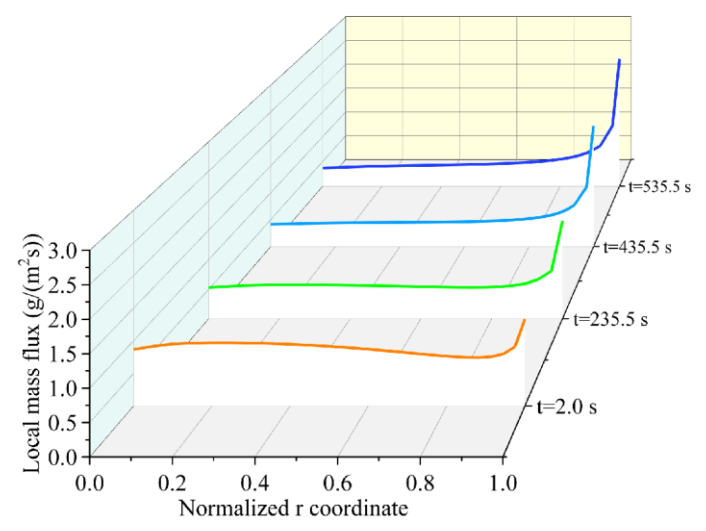


Figure 9. Local mass flux at the liquid-gas interface at different times and radial locations for case D in Table 1.

The local mass flux depends on several factors related to vapor transport, as indicated in Equation (13). Besides vapor transport considerations, evaporation requires adequate heat transfer to the liquid-vapor interface, which is governed by Equation (4). The vapor concentration, concentration gradient, and gas velocity at the interface affect evaporation flux. When the ambient humidity is constant and nearly zero (dry), the concentration gradient mainly depends on the vapor concentration and gas velocity distribution near the interface. Noting that the interface concentration is related to the interface temperature, the variation in local mass flux can be explained based on interfacial temperature and gas velocity distribution (Figure 10).

The interfacial temperature, and consequently interfacial vapor concentration, increases radially outwards, and velocity distribution along the interface is quite nonlinear. At the center of the droplet, which corresponds to the stagnation of gas flow, the mass fluxes are proportional to the temperatures. Hence, as the droplet temperature decreases, the mass flux at the center and along the interface decreases due to self-cooling. The highest mass fluxes seen near the three-phase

contact line are due to the higher temperatures at this location relative to the droplet center, which occurs due to the extremely thin contact line region, where the heat conduction from the substrate to the interface is very efficient. The computational model assumes that the flux is limited to vapor transport, which is often observed experimentally in thin film evaporation. Hence, it is expected that the finite flux evaluated in the contact line region is easily sustained by heat transfer across the droplet – physically, this would entail a slight temperature difference between the liquid-vapor interface and the substrate since the droplet thickness is relatively small. Evaporation flux, provided as an interface condition, relies on vapor concentration that depends on temperature. As we approach higher temperatures near the contact line region, the vapor concentration driving evaporation flux also increases – however, it is limited by the mass transfer rate in the gas phase. Hence, while the mass flux variation along the interface from the center to the three-phase contact line mainly depends on temperature, gas velocity can also play a minor role. For example, at t=2 s, the mass flux is maximum around the radial location of 0.2, which can be attributed to the highest gas velocities in this region that yield higher vapor advection relative to the neighboring regions.

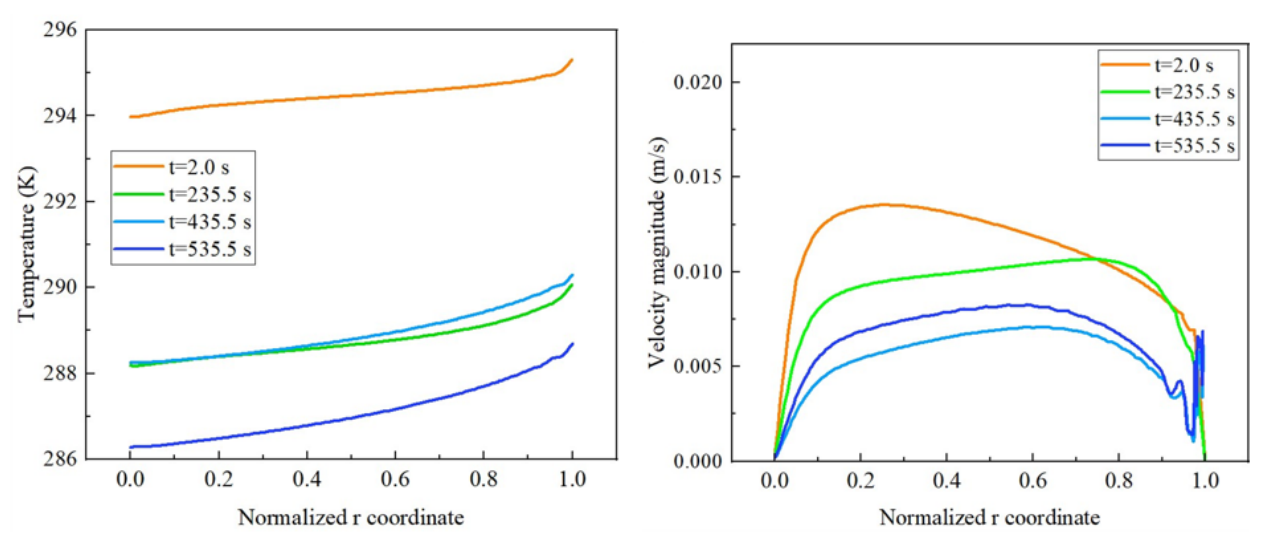


Figure 10. Temperature (left) and gas velocity (right) along the liquid-gas interface at different times (corresponding to case D in Table 1).

In addition, after transitioning to the CCA mode, a significant velocity fluctuation near the three-phase contact line is observed, as shown in Figure 10. These fluctuations can be explained by the streamlines and velocity distribution in the droplet and the gas domains, as shown in Figure 11. The magnified contact line region (labeled by the rectangular box) displays the flow characteristics, wherein the contour plot shows velocity magnitude, and the continuous lines indicate streamlines. The black arrows show the flow direction. As the contact line moves inwards toward the center of the droplet in the CCA mode, it creates a vacancy near the contact line, which is filled by the surrounding gas immediately. Consequently, an inward gas flow from the surroundings is expected near the contact line region, as indicated by the arrow along the liquid-gas interface. Besides, this movement also causes the formation of a vortex leading to velocity fluctuations near the contact line.

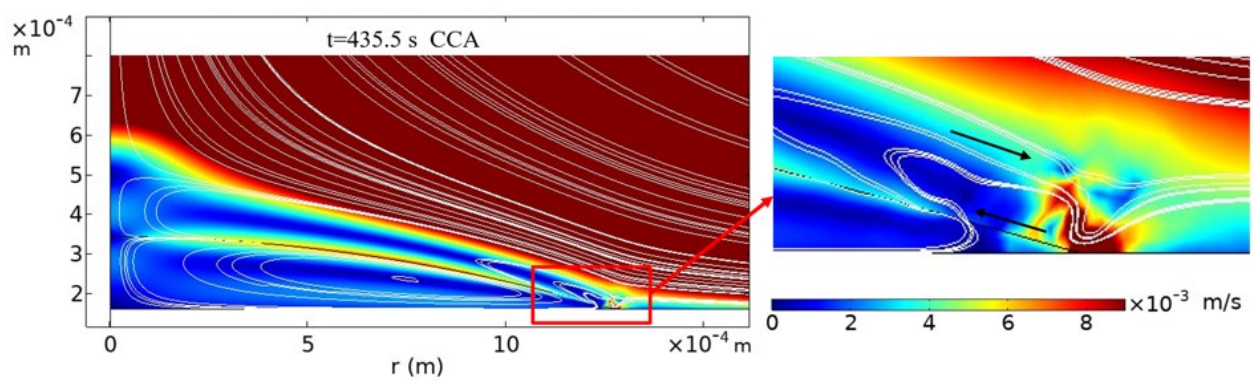


Figure 11. The velocity magnitude and streamlines for liquid and gas flow at 435.5 s (case D in Table 1). The contact line region (indicated by a rectangle) is magnified to display flow characteristics in this location. The contour plot indicates velocity magnitude (see legend), and the arrows indicate the flow directions.

# 3.4. Effect of Substrate Heating and Advection

Note that the preceding sections involve droplet evaporation when the substrate is not actively heated. However, when substrate heating is involved, it can be a primary factor influencing evaporation besides the surrounding gas flow, and this section investigates how these factors affect the evaporation time and rate. The following results are also primarily based on conditions relevant to case D. We have provided additional information where conditions depart from case D. This section assigns a heat flux at the bottom of the substrate ranging from 50 to 2000 W/m² and inlet velocities ranging from 0.4 to 3 m/s to analyze their effects on evaporation dynamics.

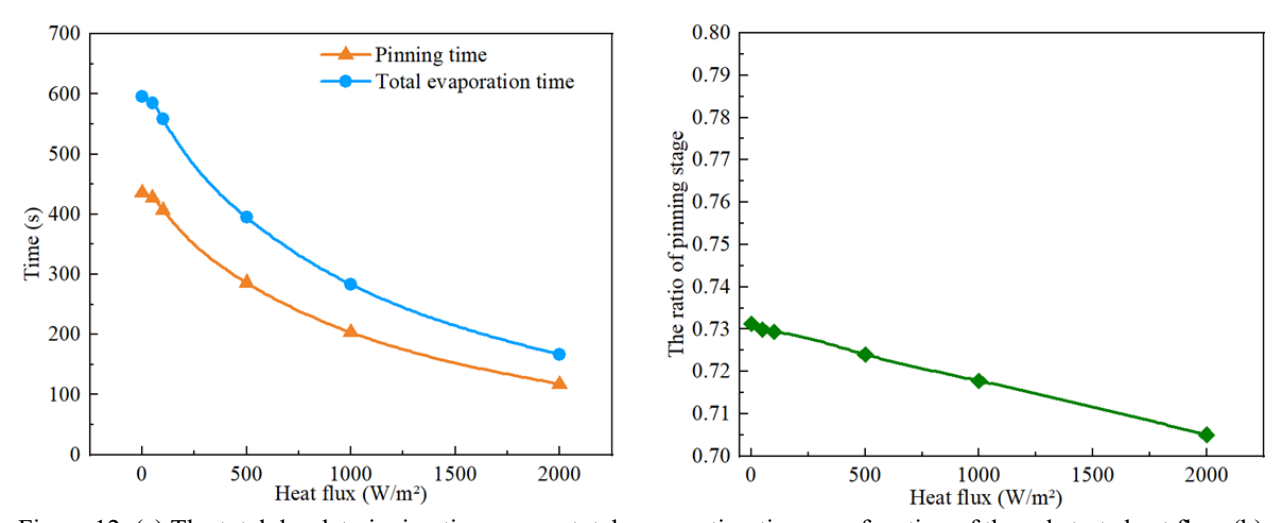


Figure 12. (a) The total droplet pinning time versus total evaporation time as a function of the substrate heat flux. (b)

The ratio of pinning time to the total evaporation time for different heat fluxes.

Figure 12 shows the total evaporation and pinning times and their ratios for different substrate heat fluxes. Here, the droplet pinning time is the duration of the CCR mode when the droplet is pinned on the substrate. The pinning and total evaporation times decrease nonlinearly with an increase in heat flux. However, the ratio of pinning to total evaporation time is nearly uniform across different substrate heat fluxes. Specifically, with a 40× increase in heat flux, we notice only

a 3% drop in the relative duration of CCR mode. This observation agrees with published experimental results [51]. Hence, while substrate heating can accelerate evaporation, it has less control over the relative durations of CCR and CCA modes. However, the relative durations can be more sensitive to the initial droplet geometry and the receding contact angle (CCR to CCA transition angle).

Figure 13a shows the temporal change in the evaporation rates for different substrate heat fluxes. For heat fluxes less than 500 W/m², there is an initial steep decline followed by a gradual decrease in the evaporation rate. The initial drop in the evaporation rate is mainly due to the change in ambient vapor concentration, which is set to zero initially in pure nitrogen. Consequently, the evaporation rate is significant in the first few seconds. The subsequent gradual reduction in the evaporation rate shows CCR mode characteristics, wherein the evaporative cooling effect supersedes the substrate heating rate, leading to a lower temperature and saturation vapor concentration at the liquid-gas interface. Afterward, evaporation enters the CCA mode with a steeper slope for the evaporation rate reduction. In CCA mode, the contact area between the droplet and the substrate decreases the heat transfer rate, while the evaporative cooling effect further lowers the droplet temperature, resulting in a rapid reduction in the evaporation rate.

When the substrate heat fluxes are higher (>500 W/m²), the evaporation rate increases sharply in the first few seconds, followed by two stages of decline corresponding to the CCR and CCA modes. The initial rise in evaporation rate is due to the large heat transfer rate from the substrate that increases the droplet temperature, which can supersede the evaporative cooling effect in the first few seconds. The rise in the evaporation rate can vary based on the applied heat flux. The evaporative cooling effect will soon dominate the rest of the evaporation process due to the limitations imposed by the thermal conduction resistance of the substrate and the droplet. Subsequent variations in droplet evaporation rates with the two characteristic slopes correspond to the CCR and CCA modes of evaporation described above.

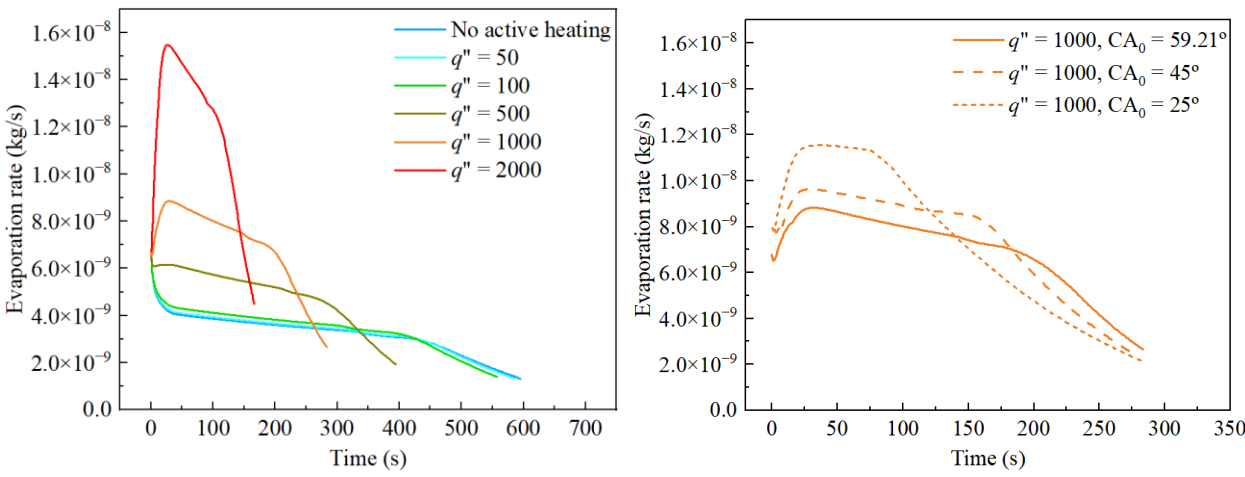


Figure 13. (a) The evaporation rate versus time for different substrate heat fluxes (in W/m<sup>2</sup>). (b) Droplet evaporation rate as a function of time and initial (equilibrium) contact angles for (a) substrate heated at  $q'' = 1000 \text{ W/m}^2$ .

These results are instructive in tailoring conditions for controlling evaporation in some applications. For example, applying a heat flux is a simple technique to accelerate evaporation,

which for example, is carried out on rearview mirrors and windscreens in automobiles using resistive heating. However, surface heating alone cannot guarantee high evaporation rates since surface wettability also controls evaporation kinetics. The decrease in evaporation rate resulting from a shrinking contact area shows that droplets with a lower equilibrium and receding contact angles will generally promote evaporation. For example, Figure 13b compares evaporation rates of droplets with similar initial volume and receding contact angle (case D) but different equilibrium angles. As expected, smaller equilibrium contact angles yield higher average evaporation rates and smaller droplet lifetimes. Hence, besides controlling heat flux, surface engineering can help tune wettability towards a more wetting state and sustain high evaporation rates. In order to explore how gas flow affects the evaporation dynamics of the droplet, inlet velocities ranging from 0.4 m/s (case D) to a maximum value of 3 m/s were explored. The Reynolds number (Re) corresponding to these conditions is  $Re = \rho V L/\mu$ , where  $\rho$  is the density of the gas, V is the inlet velocity, L is the radius of the inlet, and  $\mu$  is the dynamic viscosity of the gas. This model explores Re from 318 to 2384.

Figure 14a shows the total evaporation and pinning times and their ratios as a function of *Re*. While the pinning and total evaporation times decrease with *Re*, some similarities to the effects of substrate heat flux are seen here. The ratio of pinning time to total evaporation time is independent of *Re* as well, as shown in Figure 14b. Hence, while the total evaporation time can be reduced by increasing the inlet velocity, vapor advection does not significantly affect the relative durations of the CCR and CCA evaporation modes.

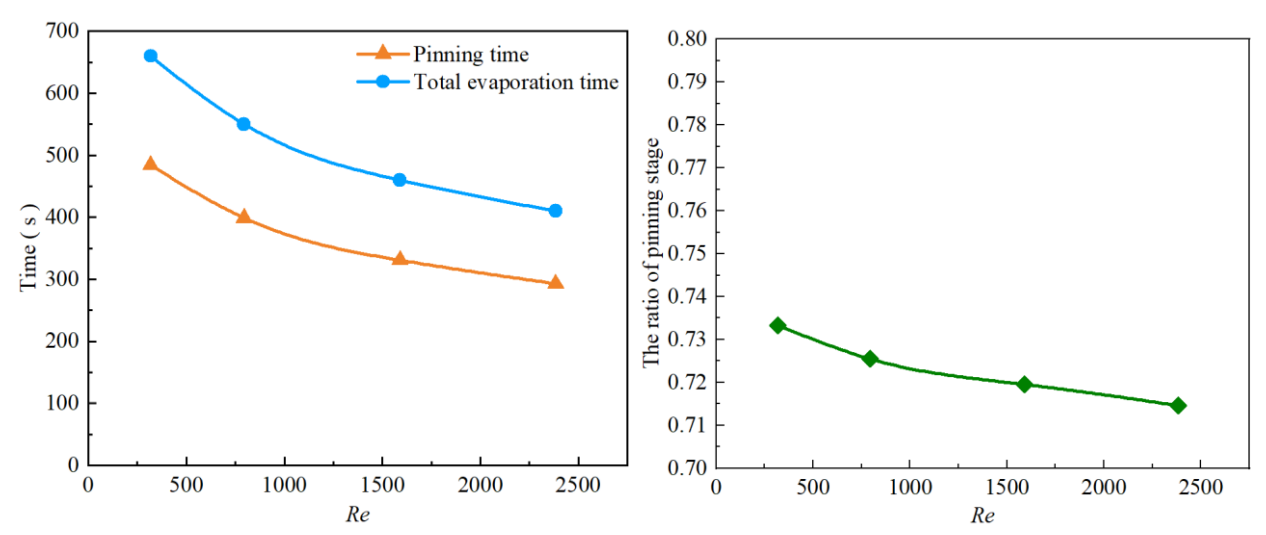


Figure 14. (a) The total evaporation and droplet pinning time as a function of inlet air velocity (Reynolds number, *Re*). (b) The ratio of pinning time to the total evaporation time as a function of the inlet velocity (*Re*).

Figure 15a shows the instantaneous evaporation rate for different Re. The evaporation rate versus Re resembles the case of droplet evaporation with low substrate heat flux ( $<500 \text{ W/m}^2$ ) where the evaporation rate dramatically drops in the first few seconds, then reduces gradually for CCR mode, followed by a more rapid decrease for the CCA-mode evaporation. Generally, the evaporation rate increases with an increase in Re due to higher vapor transport in the gas phase, even though the simulated range of Re is not as effective in improving the evaporation rate as

applying higher substrate heat fluxes. As seen earlier with active heating, a lower equilibrium contact angle for droplets with similar initial volumes and receding contact angles correspond to higher average evaporation rates (Figure 15b). This phenomenon involving no active heating but a fluid stream for drying is also relevant in many applications like dehydration in food packaging and semiconductor fabrication. Understanding how flow conditions and surface wettability influences evaporation dynamics can help avoid undesirable effects such as bacterial growth in food production and defects in semiconductors.

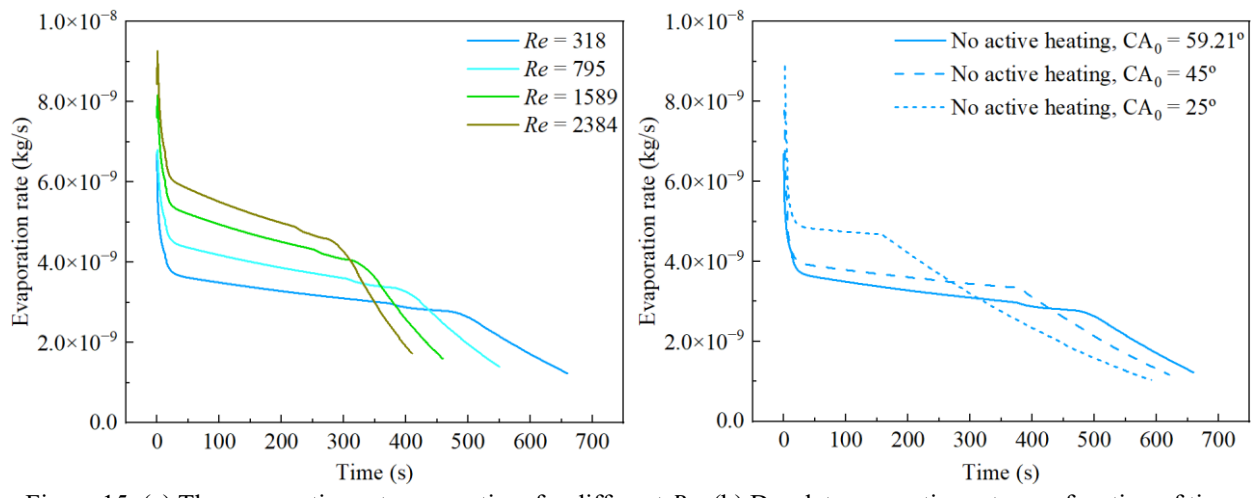


Figure 15. (a) The evaporation rate versus time for different Re. (b) Droplet evaporation rate as a function of time and initial (equilibrium) contact angles for an unheated substrate and Re = 318.

#### 4. Conclusions

This study uses an unsteady two-step arbitrary Lagrangean-Eulerian (ALE) moving mesh model to simulate evaporation in the constant contact radius (CCR) and constant contact angle (CCA) modes for a sessile water droplet on a quartz substrate. The automatic re-mesh is applied to the model to maintain mesh quality during the large deformation of the droplet during evaporation. Vapor transport in the gas domain, fluid flow in the gas and liquid domains, and heat transfer in all three domains were coupled in this model to solve the vapor concentration, velocity, and temperature distributions. In addition, the model includes Marangoni flow due to temperature-dependent surface tension, convective mass flux due to the ambient gas flow, and the effect of evaporative cooling. The ALE moving mesh tracks the sharp liquid-gas interface, and the force balance at the interface directly determines the droplet shape. Therefore, the model applies to both spherical and nonspherical drops and is generally applicable for sessile droplet evaporation for various single-component liquid droplets, substrate materials, and surrounding gases.

The experimentally validated model predicts evaporation in the CCR mode, followed by the CCA mode. The contact radius, contact angle, and droplet volume of simulation results agree well with those seen in the experiments. Furthermore, the droplet and substrate temperature distribution, the velocity field inside the droplet, and the interfacial local mass flux and temperature are studied. The droplet and the substrate are initially of uniform ambient temperature. In an unheated substrate, the average temperature of the droplet decreases and then increases slightly in CCR mode due to

the competing effects between evaporative cooling and the thermal resistance from the substrate to the liquid-gas interface. However, the average temperature of the droplet decreases in the CCA mode due to a shrinking contact area. The Marangoni flow leads to multiple vortices within the droplet, with a single vortex surviving for the majority of the droplet's lifetime during evaporation.

The local mass flux along the liquid-gas interface depends on the liquid velocity magnitude and the interface temperature, with higher velocity magnitudes and interface temperatures leading to larger local mass fluxes. Besides, substrate heating and inlet air velocity also influence the evaporative dynamics. The evaporation time can be dramatically reduced by either increasing the substrate heat flux or the inlet velocity. However, these two factors do not significantly affect the relative durations of CCR and CCA evaporation modes.

# **Acknowledgments**

S. Narayan acknowledges the support from the National Science Foundation's Division of Chemical, Bioengineering, Environmental, and Transport Systems in the Directorate for Engineering under Grant No. 1944323.

#### References

- [1] V. Dugas, J. Broutin, E. Souteyrand, Droplet Evaporation Study Applied to DNA Chip Manufacturing, Langmuir, 21(20) (2005) 9130-9136.
- [2] W. Cheng, W. Zhang, H. Chen, L. Hu, Spray cooling and flash evaporation cooling: The current development and application, Renewable and Sustainable Energy Reviews, 55 (2016) 614-628.
- [3] Z. Lu, S. Narayanan, E.N. Wang, Modeling of evaporation from nanopores with nonequilibrium and nonlocal effects, Langmuir, 31(36) (2015) 9817-9824.
- [4] D.F. Hanks, Z. Lu, S. Narayanan, K.R. Bagnall, R. Raj, R. Xiao, R. Enright, E.N. Wang, Nanoporous evaporative device for advanced electronics thermal management, in: Fourteenth Intersociety Conference on Thermal and Thermomechanical Phenomena in Electronic Systems (ITherm), IEEE, 2014, pp. 290-295.
- [5] H. Minemawari, T. Yamada, H. Matsui, J.y. Tsutsumi, S. Haas, R. Chiba, R. Kumai, T. Hasegawa, Inkjet printing of single-crystal films, Nature, 475(7356) (2011) 364-367.
- [6] N. Belmiloud, A.-H. Tamaddon, P. Mertens, H. Struyf, X. Xu, Dynamics of the drying defects left by residual ultra-pure water droplets on silicon substrate, ECS Journal of Solid State Science and Technology, 1(1) (2012) P34.
- [7] J.Y. Zhang, M. Mahalanabis, L. Liu, J. Chang, N.R. Pollock, C.M. Klapperich, A disposable microfluidic virus concentration device based on evaporation and interfacial tension, Diagnostics, 3(1) (2013) 155-169.
- [8] M. Gibbons, P. Di Marco, A. Robinson, Local heat transfer to an evaporating superhydrophobic droplet, International Journal of Heat and Mass Transfer, 121 (2018) 641-652.
- [9] M.E. Shanahan, Simple theory of "stick-slip" wetting hysteresis, Langmuir, 11(3) (1995) 1041-1043.

- [10] B. Zuo, F.F. Zheng, Y.R. Zhao, T. Chen, Z.H. Yan, H. Ni, X. Wang, Stick-slip phenomenon in measurements of dynamic contact angles and surface viscoelasticity of poly (styrene-bisoprene-b-styrene) triblock copolymers, Langmuir, 28(9) (2012) 4283-4292.
- [11] N. Kovalchuk, A. Trybala, V. Starov, Evaporation of sessile droplets, Current Opinion in Colloid & Interface Science, 19(4) (2014) 336-342.
- [12] R. Picknett, R. Bexon, The evaporation of sessile or pendant drops in still air, Journal of colloid and Interface Science, 61(2) (1977) 336-350.
- [13] K. Sefiane, R. Bennacer, An expression for droplet evaporation incorporating thermal effects, Journal of Fluid Mechanics, 667 (2011) 260-271.
- [14] P.L. Kelly-Zion, C.J. Pursell, N. Hasbamrer, B. Cardozo, K. Gaughan, K. Nickels, Vapor distribution above an evaporating sessile drop, International Journal of Heat and Mass Transfer, 65 (2013) 165-172.
- [15] L. Bin, R. Bennacer, A. Bouvet, Evaporation of methanol droplet on the Teflon surface under different air velocities, Applied Thermal Engineering, 31(17) (2011) 3792-3798.
- [16] Y. Tsoumpas, S. Dehaeck, A. Rednikov, P. Colinet, Effect of Marangoni Flows on the Shape of Thin Sessile Droplets Evaporating into Air, Langmuir, 31(49) (2015) 13334-13340.
- [17] W. Shi, K. Tang, J. Ma, Y. Jia, H. Li, L. Feng, Marangoni convection instability in a sessile droplet with low volatility on heated substrate, International Journal of Thermal Sciences, 117 (2017) 274-286.
- [18] H. Hu, R.G. Larson, Evaporation of a sessile droplet on a substrate, The Journal of Physical Chemistry B, 106(6) (2002) 1334-1344.
- [19] S. Semenov, V.M. Starov, R.G. Rubio, M.G. Velarde, Instantaneous distribution of fluxes in the course of evaporation of sessile liquid droplets: Computer simulations, Colloids and Surfaces A: Physicochemical and Engineering Aspects, 372(1) (2010) 127-134.
- [20] S. Semenov, V. Starov, R. Rubio, M. Velarde, Computer simulations of quasi-steady evaporation of sessile liquid droplets, Trends in Colloid and Interface Science XXIV, (2011) 115-120.
- [21] D. Hu, H. Wu, Numerical study and predictions of evolution behaviors of evaporating pinned droplets based on a comprehensive model, International Journal of Thermal Sciences, 96 (2015) 149-159.
- [22] Z. Pan, J.A. Weibel, S.V. Garimella, Transport mechanisms during water droplet evaporation on heated substrates of different wettability, International Journal of Heat and Mass Transfer, 152 (2020) 119524.
- [23] F. Kang, Y. Shen, Y. Cheng, N. Li, Lifetime Prediction of Sessile Droplet Evaporation with Coupled Fields, Industrial & Engineering Chemistry Research, 60(43) (2021) 15782-15792.
- [24] B. Murray, M.J. Fox, S. Narayan, Analyzing interfacial transport for water evaporating into dry nitrogen, Applied Thermal Engineering, 202 (2022) 117910.
- [25] X. Shang, X. Zhang, T.-B. Nguyen, T. Tran, Direct numerical simulation of evaporating droplets based on a sharp-interface algebraic VOF approach, International Journal of Heat and Mass Transfer, 184 (2022) 122282.

- [26] N. Murisic, L. Kondic, On evaporation of sessile drops with moving contact lines, Journal of fluid mechanics, 679 (2011) 219-246.
- [27] J. Shaikh, A. Sharma, R. Bhardwaj, On sharp-interface dual-grid level-set method for two-phase flow simulation, Numerical Heat Transfer, Part B: Fundamentals, 75(1) (2019) 67-91.
- [28] M. Ben Said, M. Selzer, B. Nestler, D. Braun, C. Greiner, H. Garcke, A phase-field approach for wetting phenomena of multiphase droplets on solid surfaces, Langmuir, 30(14) (2014) 4033-4039.
- [29] C.W. Hirt, B.D. Nichols, Volume of fluid (VOF) method for the dynamics of free boundaries, Journal of Computational Physics, 39(1) (1981) 201-225.
- [30] J. Reutzsch, C. Kieffer-Roth, B. Weigand, A consistent method for direct numerical simulation of droplet evaporation, Journal of Computational Physics, 413 (2020) 109455.
- [31] M. Irfan, M. Muradoglu, A front tracking method for direct numerical simulation of evaporation process in a multiphase system, Journal of Computational Physics, 337 (2017) 132-153.
- [32] G. Lupo, M.N. Ardekani, L. Brandt, C. Duwig, An immersed boundary method for flows with evaporating droplets, International Journal of Heat and Mass Transfer, 143 (2019) 118563.
- [33] K. Yang, F. Hong, P. Cheng, A fully coupled numerical simulation of sessile droplet evaporation using Arbitrary Lagrangian–Eulerian formulation, International Journal of Heat and Mass Transfer, 70 (2014) 409-420.
- [34] Y. Chen, W. Hu, J. Wang, F. Hong, P. Cheng, Transient effects and mass convection in sessile droplet evaporation: The role of liquid and substrate thermophysical properties, International Journal of Heat and Mass Transfer, 108 (2017) 2072-2087.
- [35] H. Jia, X. Xiao, Y. Kang, Investigation of a free rising bubble with mass transfer by an arbitrary Lagrangian–Eulerian method, International Journal of Heat and Mass Transfer, 137 (2019) 545-557.
- [36] Y. Chen, F. Hong, P. Cheng, Transient flow patterns in an evaporating sessile drop: A numerical study on the effect of volatility and contact angle, International Communications in Heat and Mass Transfer, 112 (2020) 104493.
- [37] H. Muramatsu, A.L. Pillai, K. Kitada, R. Kurose, Numerical simulation of bi-component fuel droplet evaporation using Level Set method, Fuel, 318 (2022) 123331.
- [38] P. Sáenz, K. Sefiane, J. Kim, O. Matar, P. Valluri, Evaporation of sessile drops: a three-dimensional approach, Journal of Fluid Mechanics, 772 (2015) 705-739.
- [39] C. Zhang, H. Zhang, X. Zhang, C. Yang, P. Cheng, Evaporation of a sessile droplet on flat surfaces: An axisymmetric lattice Boltzmann model with consideration of contact angle hysteresis, International Journal of Heat and Mass Transfer, 178 (2021) 121577.
- [40] J. Yu, R. Tang, Y. Li, L. Zhang, C. Wu, Molecular dynamics simulation of heat transport through solid–liquid interface during argon droplet evaporation on heated substrates, Langmuir, 35(6) (2019) 2164-2171.

- [41] C. Doursat, L. Lecoq, O. Laguerre, D. Flick, Droplet evaporation on a solid surface exposed to forced convection: Experiments, simulation and dimensional analysis, International Journal of Heat and Mass Transfer, 113 (2017) 1234-1245.
- [42] S. Narayanan, A.G. Fedorov, Y.K. Joshi, Experimental characterization of a micro-scale thin film evaporative cooling device, in: 2010 12th IEEE Intersociety Conference on Thermal and Thermomechanical Phenomena in Electronic Systems, IEEE, 2010, pp. 1-10.
- [43] Z. Lu, T.R. Salamon, S. Narayanan, K.R. Bagnall, D.F. Hanks, D.S. Antao, B. Barabadi, J. Sircar, M.E. Simon, E.N. Wang, Design and modeling of membrane-based evaporative cooling devices for thermal management of high heat fluxes, IEEE transactions on components, packaging and manufacturing technology, 6(7) (2016) 1056-1065.
- [44] B. Murray, M.J. Fox, S. Narayanan, Quantifying the evaporation rate of sessile droplets using a quartz crystal microbalance, Journal of Applied Physics, 128(3) (2020) 035101.
- [45] Z. Lin, R.M. Hill, H.T. Davis, M.D. Ward, Determination of wetting velocities of surfactant superspreaders with the quartz crystal microbalance, Langmuir, 10(11) (1994) 4060-4068.
- [46] Z. Lin, M.D. Ward, The role of longitudinal waves in quartz crystal microbalance applications in liquids, Analytical Chemistry, 67(4) (1995) 685-693.
- [47] B. Murray, S. Narayanan, The role of wettability on the response of a quartz crystal microbalance loaded with a sessile droplet, Scientific reports, 9(1) (2019) 17289.
- [48] A. Hillier, M. Ward, Scanning electrochemical mass sensitivity mapping of the quartz crystal microbalance in liquid media, Analytical Chemistry, 64(21) (1992) 2539-2554.
- [49] Moist air water vapor and saturation pressure, in, Engineering ToolBox, 2004.
- [50] T.L. Bergman, T.L. Bergman, F.P. Incropera, D.P. Dewitt, A.S. Lavine, Fundamentals of heat and mass transfer, John Wiley & Sons, 2011.
- [51] M. Gao, P. Kong, L.-X. Zhang, J.-N. Liu, An experimental investigation of sessile droplets evaporation on hydrophilic and hydrophobic heating surface with constant heat flux, International Communications in Heat and Mass Transfer, 88 (2017) 262-268.